Electric supplementary information (ESI)

Unraveling the kinetics of structural development during polymerization-induced self-assembly: Decoupling the polymerization and the micelle structure

Rintaro Takahashi,[‡a] Shotaro Miwa, [‡a] Fabian H. Sobotta,[bc] Ji Ha Lee,[a] Shota Fujii,[a] Noboru Ohta,[d] Johannes C. Brendel,[*bc] Kazuo Sakurai[*a]

[a]*Department of Chemistry and Biochemistry, University of Kitakyushu, 1-1 Hibikino, Wakamatsu-ku, Kitakyushu, Fukuoka 808-0135, Japan*
[b]*Laboratory of Organic and Macromolecular Chemistry (IOMC), Friedrich Schiller University Jena, Humboldtstrasse 10, 07743 Jena, Germany*
[c]*Jena Center for Soft Matter (JCSM), Friedrich Schiller University Jena, Philosophenweg 7, 07743 Jena, Germany*
[d]*Japan Synchrotron Radiation Research Institute (JASRI/SPring-8), 1-1-1 Kouto, Sayo, Sayo, Hyogo 679-5198, Japan*

[‡]*These authors contributed equally to this work.*
**E-mail: (K.S.)* sakurai@kitakyu-u.ac.jp *and (J. C. B.)* johannes.brendel@uni-jena.de.

Table of Contents

SEC Results. The *ex situ* SEC measurements of the polymerization kinetics were performed using a Shimadzu system equipped with a SCL-10A system controller, a LC-10AD pump, a RID-10A refractive index detector and a PSS SDV column with *N*,*N*-dimethylacetamide (DMAc) + 0.21% LiCl as eluent. This eluent dissolves PNAT-*b*-PNAM molecularly.[S1] The column oven was set to 50 °C. The polymerization was performed in a microwave vial at T = 70, 80 and 90 °C and a concentration of 0.01wt%. Prior to polymerization the solution was deoxygenated by a stream of nitrogen for 20 min. After different time points, samples (1 mL) were taken from the polymerization mixture, directly frozen and lyophilized. The residual polymer was dissolved in the eluent (700 μL) and SEC was measured to determine the size distribution. Figs. S1 and S2 show the SEC chromatograms and the dispersity index.

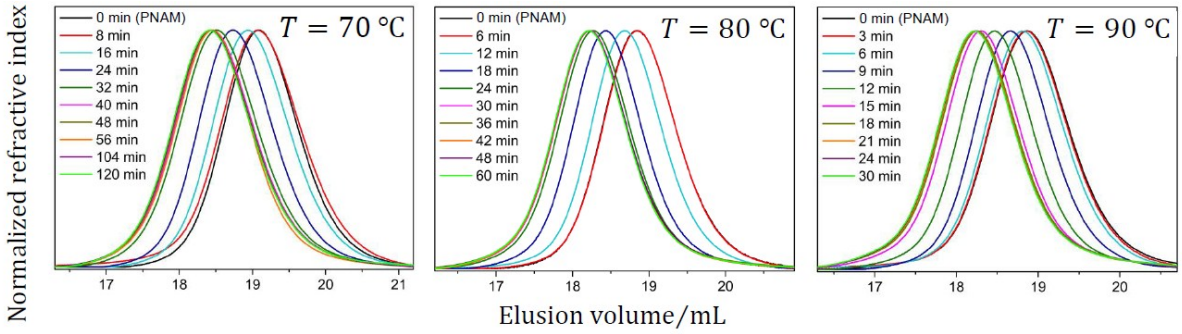

Fig. S1 SEC chromatograms at each time during the polymerization at T = 70 °C (left), 80 °C (center), and 90 °C (right).

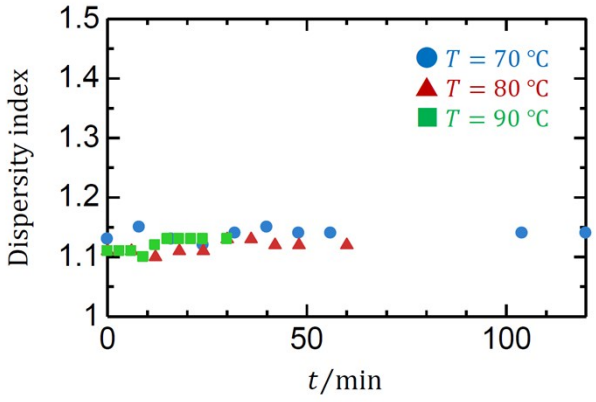

Fig. S2 The dispersity index of the single polymer chain ($M_{w,1}/M_{n,1}$) as a function of time at T = 70 °C (blue circle), 80 °C (red triangle), and 90 °C (green square).

NMR Spectra. Fig. S3 shows the time evolution of the NMR spectra at T = 70 °C. Each peak can be assigned to the proton indicated as the corresponding numeric character in the chemical structure. In particular, the peaks from the vinyl protons of the NAT monomer were observed around the chemical shift of 6 ppm. As the polymerization proceeds, these peaks decrease, and the conversion was estimated from the area. In this estimation of the area, the Gaussian distribution was used to separate the peaks, as shown in Fig. S3a.

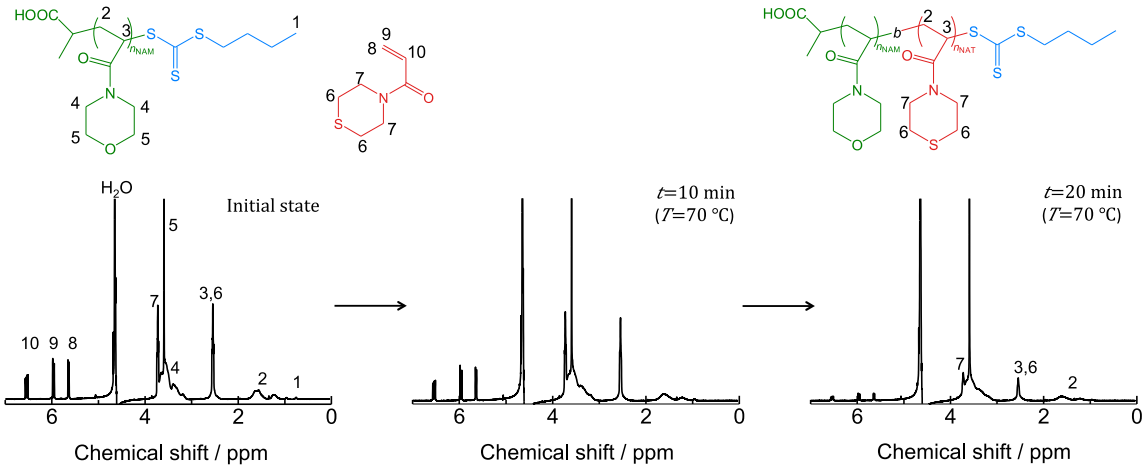

Fig. S3a NMR spectra at the initial state (left), t = 10 min (center) and 20 min (right) at T = 70 °C in D_2O.

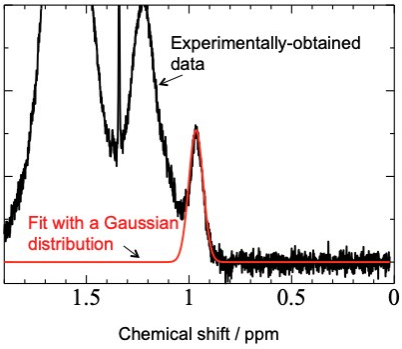

Fig. S3b Magnified NMR spectrum at t = 20 min and at 70 °C. Black and red curves represent the experimentally-obtained data and the fitted curve (Gaussian distribution), respectively.

Kinetic Model of RAFT Polymerization. RAFT polymerization is composed of initiation (including the decomposition of initiator and the reaction of initiator and monomer), propagation, and termination,[S2] which can be expressed by

$$I_2 \xrightarrow{k_d} 2I^{\bullet} \tag{S1}$$

$$I^{\bullet} + M \xrightarrow{k_i} P_1^{\bullet} \tag{S2}$$

$$P_n^{\bullet} + M \xrightarrow{k_p} P_{n+1}^{\bullet} \tag{S3}$$

$$P_n^{\bullet} + P_m^{\bullet} \xrightarrow{k_t} P_n + P_m \tag{S4}$$

Here, I_2, M, and P_n represent the initiator, the monomer (NAT), and the polymer with the degree of polymerization of n, respectively. k_d, k_i, k_p, and k_t are the kinetic constants of the respective reactions. Within the initiation [decomposition of initiator (eq S1) and the reaction between the initiator and monomer (eq S2)], k_d is normally much smaller than k_i. *ie.,* the decomposition of the initiator is the rate-limiting process at this stage; thus, the reaction between the initiator and monomer (eq S2) can be ignored. The kinetic equations for eqs S1, S3, and S4 are given by

$$\frac{dC_{I_2}}{dt} = -2k_d f C_{I_2} \tag{S5}$$

$$\frac{dC_M}{dt} = -k_p C_M C_{P^{\bullet}} \tag{S6}$$

$$\frac{dC_{P^{\bullet}}}{dt} = -2k_t C_{P^{\bullet}}^2 \tag{S7}$$

where f is the efficiency of the initiator, and C_{I_2}, C_M, and $C_{P^{\bullet}}$ are the concentrations of the initiator, monomer, and polymer, respectively.

It is known that retardations happen in RAFT polymerizations[S2]. More specifically, (i) a propagation rate of RAFT is slower than that of a conventional radical polymerization. (ii) An induction time is observed before propagation process, which is caused by initiation process of RAFT polymerization. These effects may be taken into

account as follows: The former effect can be included in k_p, and k_p is thus the *apparent* kinetic constant. The latter effect can be considered by using the induction time (t_{ind}; *cf.* the main text) as a adjustable parameter. Although detailed models of retardation effects in view of molecular mechanisms are proposed,[S2] we use the above three reactions (eqs S1, S3, and S4) with t_{ind} in the present study for the simplicity.

By solving the eq S5, we obtain

$$C_{I_2}(t) = C_{I_2}(0)\exp\left(-k_d t\right) \tag{S8}$$

Whilst, concerning eqs S5−S7, we have eq S9 by assuming that the initiation rate is the same as the termination rate because of the constant radial concentration during the polymerization.

$$C_{P^\bullet} = \sqrt{\frac{k_d f}{k_t} C_{I_2}} \tag{S9}$$

Thus, the reaction rate of the monomer can be expressed by

$$\frac{dC_M}{dt} = -k_p C_M \sqrt{\frac{k_d f}{k_t} C_{I_2}(0)\exp\left(-k_d t\right)} \tag{S10}$$

By solving this differential equation, we can express C_M as a function of time (eq 1 in the main text). Here, C_M corresponds to C_{NAT}. $C_{NAT}(t)$ is related to the weight fraction (w_{NAT}) of the monomer (NAT) within the solute by

$$w_{NAT}(t) = \frac{C_{NAT}(t) M_{NAT}}{C_{PNAM}(M_{n,PNAT}(t) + M_{n,PNAM}) + C_{NAT}(t) M_{NAT}} \tag{S11}$$

Livingness. According to the literature,[S2] the number fraction of the living chains (so-called livingness; denoted as L) can be calculated by

$$L = \frac{C_{PNAM}}{C_{PNAM} + 2fC_{I_2}(0)\left[1 - \exp(-k_d t)\right]} \tag{S12}$$

This equation assumes that the termination event occurs only through bimolecular termination by disproportionation. In the calculation of L, $f = 0.5$ was used, and k_d was calculated using the Arrhenius-type activation energy, as in the calculation of $p(t)$ with eq 1 (see the main text).

Rate of Micellar Formation/Growth. Table S1 lists literatures concerning the kinetics of micellar formation or growth in block copolymers. Except for the atypical cases,[S4,S11] the micelle formation or growth usually may complete within one second.[S3,S5−S10,S12]

Table S1. Literatures Concerning the Kinetics of Micellar Formation/Micellar Growth.

Polymer/Solvent	Method	Equilibrium arrival time / s	Ref.
PS_{424}-*b*-PEP_{870}[a]/dioxane-heptane PS_{100}-*b*-PHB_{1900}-*b*-PS_{100}[b]/dioxane-heptane	Stopped-flow; light scattering	0.5	Ref. S3
$PaMS_{598}$-*b*-$PVPA_{74}$[c]/Benzyl alcohol $PaMS_{958}$-*b*-$PVPA_{83}$[c]/Benzyl alcohol	Temperature jump; light scattering	10^6	Ref. S4
PEO_{97}-*b*-PPO_{69}-*b*-PEO_{97}[d]/water PEO_{20}-*b*-PPO_{69}-*b*-PEO_{20}[d]/water PEO_{100}-*b*-PPO_{39}-*b*-PEO_{100}[d]/water	Temperature-jump; light scattering	0.05	Ref. S5
PEO_{19}-*b*-PPO_{43}-*b*-PEO_{19}[d]/water PEO_{26}-*b*-PPO_{40}-*b*-PEO_{26}[d]/water PEO_{17}-*b*-PPO_{60}-*b*-PEO_{17}[d]/water PEO_{27}-*b*-PPO_{61}-*b*-PEO_{27}[d]/water PEO_{132}-*b*-PPO_{50}-*b*-PEO_{132}[d]/water	Temperature-jump; light scattering	0.02	Ref. S6
PEO_{13}-*b*-PPO_{30}-*b*-PEO_{13}[d]/water	Temperature-jump; light scattering	0.01	Ref. S7
PEO_{13}-*b*-PPO_{30}-*b*-PEO_{13}[d]/water	Temperature-jump; light scattering	0.1	Ref. S8
$PGMA_{45}$-*b*-$PDMA_{34}$-*b*-$PDEA_{52}$[e]/water	Stopped-flow; light scattering	1	Ref. S9, S10
PEP_{16}-*b*-PEO_{497}[f]/water-DMF	Stopped-flow; SAXS	50	Ref. S11
PEO_{114}-*b*-PCL_{32}[g]/water-THF	Microfluidic device; SAXS	0.5	Ref. S12

[a]polystyrene-*b*-poly(ethylene-propylene) [b]polystyrene-*b*-poly(hydrogenerted butadiene)-*b*-polystyrene [c]poly(*α*-methylstyrene)-*b*-poly(vinylphenethyl alcohol) [d]poly(ethylene oxide)-*b*-poly(propylene oxide)-*b*-poly(ethylene oxide) [e]poly(glycerol monomethacrylate)-*b*-poly[2-(dimethylamino)ethyl methacrylate]-*b*-poly[2-(diethylamino) ethyl methacrylate] [f]poly(ethylene-*alt*-polypropylene)-*b*-poly(ethylene oxide) [g]poly(ethylene oxide)-*b*-poly(caprolactone)

Time-Evolution of the Kratky Plots. Time-evolution of Kratky plots during PISA at each temperature are shown in Fig. S4. In the initial state (gray symbols), no peaks are observed, and we can see the plateau at higher q range (q > 1 nm^{-1}). This plateau indicates the scattering from flexible chains. As time passes, a peak appears around q = 0.2 nm^{-1} at all the temperature, demonstrating the self-assembly proceeds in the solution. Whereas, the plateau at higher q region is still observed, which indicate the flexible chains are present in the particle interface (*ie.*, the core-corona structure is formed), or not-assembled chains are present.

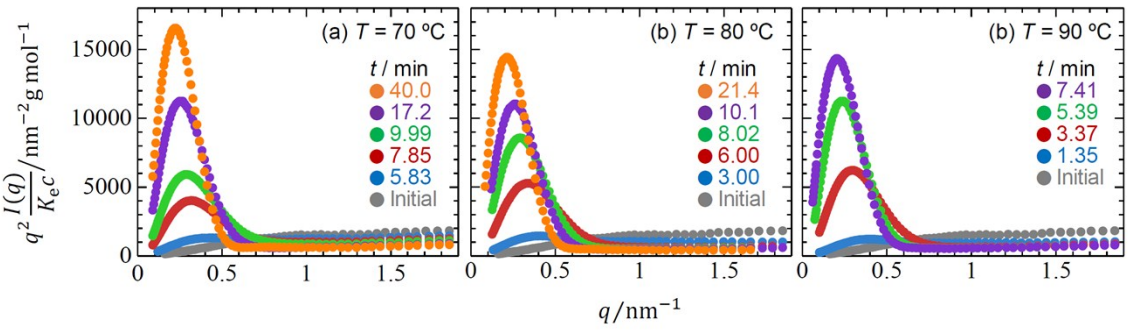

Fig. S4 Time-evolution of the SAXS data as Kratky plots during PISA at 70 °C (a), 80 °C (b), and 90 °C.

Analysis of the SAXS profiles − The form factor of micelle. The SAXS profiles were analyzed by eq 2 in the main text.[S13] In that equation, γ_{poly} is the contrast factor of the polymer which can be calculated from the contrast factor of NAM block (γ_{NAM}) and NAT block (γ_{NAT}) by:

$$\gamma_{\mathrm{poly}}(t) = \frac{M_{\mathrm{n,PNAT}}(t)\gamma_{\mathrm{NAT}} + M_{\mathrm{n,PNAM}}\gamma_{\mathrm{NAM}}}{M_{\mathrm{n,PNAM}\text{-}b\text{-}\mathrm{PNAT}}(t)} \tag{S13}$$

$w_{\mathrm{NAT}}(t)$ and $\gamma_{\mathrm{poly}}(t)$ are the time dependent quantities, but once the time dependence of $M_{\mathrm{n,PNAT}}(t)$ is determined by NMR measurements, $w_{\mathrm{NAT}}(t)$ and $\gamma_{\mathrm{poly}}(t)$ are obtained as functions of time by eqs S11 and S13, which enables in decreasing the number of the adjustable parameters in the fitting of the SAXS profiles.

Regarding $P_{\mathrm{z,mic}}(q)$, we used the model form factor of a spherical micelle (composed of uniform-density spherical core and coronal Gaussian chains), which is given by eq 3 in the main text.[S14] In that equation, $E_{\mathrm{ch}}(q)$ denotes the time-averaged amplitudes of the scattering electric field from each coronal chain, given by

$$E_{\mathrm{ch}}^2(q) = \frac{2\left[\exp\left(-q^2 {R_{\mathrm{g,S}}}^2\right) - 1 + q^2 {R_{\mathrm{g,S}}}^2\right]}{q^4 {R_{\mathrm{g,S}}}^4} \exp\left(-d^2 q^2 / 16\right) \tag{S14}$$

Here, d is the cross-sectional diameter of the coronal chain. f_{C} in eq 3 is the contrast of the core domain within the micelle, defined by

$$f_{\mathrm{C}}(t) = \frac{\gamma_{\mathrm{NAT}} M_{\mathrm{n,PNAT}}(t)}{\gamma_{\mathrm{NAT}} M_{\mathrm{n,PNAT}}(t) + \gamma_{\mathrm{NAM}} M_{\mathrm{n,PNAM}}} \tag{S15}$$

f_{C} can be calculated because $M_{\mathrm{n,PNAT}}(t)$ is known by eq 6 in the main text. Therefore, N_{agg} and R_{C} can be determined by the fitting of the SAXS profiles.

Here, R_{C} is related to the molar mass (M_{mic}) by

$$\frac{4\pi R_{\mathrm{C}}^3}{3} = \frac{w_{\mathrm{C}} M_{\mathrm{mic}}}{N_{\mathrm{Av}} c_{\mathrm{w,NAT}}} \tag{S16}$$

ie., $P_{\mathrm{mic}}(q)$ is a function of M_{mic}. To take into account the dispersity in the fitting of the SAXS profile, a log-normal distribution for M was assumed by[S13]

$$M_{\mathrm{w,mic}} P_{\mathrm{z,mic}}(q) = \frac{\int P_{\mathrm{mic}}(q) \exp\left[-\frac{\ln^2\left(M / \sqrt{M_{\mathrm{w,mic}} M_{\mathrm{n,mic}}}\right)}{2\ln(M_{\mathrm{w,mic}} / M_{\mathrm{n,mic}})}\right] \mathrm{d}M}{\sqrt{2\pi \ln(M_{\mathrm{w,mic}} / M_{\mathrm{n,mic}})}} \tag{S17}$$

The subscript notations of 'n', 'w', and 'z' denote the number-average, weight-average, and z-average quantities. The R_{C} values shown in Figs. 4 and 5 are the averages values calculated with the weight-average molar mass of the micelle ($M_{\mathrm{w,mic}}$) by

$$\left\langle R_{\mathrm{C}} \right\rangle \equiv \sqrt[3]{\frac{w_{\mathrm{core}} M_{\mathrm{w,mic}}}{N_{\mathrm{A}} c_{\mathrm{w,NAT}}}} \tag{S18}$$

For the simplicity, $\left\langle R_{\mathrm{C}} \right\rangle$ is denoted as R_{C} in the main text.

In this model, the effect of the encapsulation of unreacted monomer (NAT) into the micellar core during PISA is omitted for the simplicity. If a non-negligible encapsulation takes place, the micellar structure (size) and the kinetics of polymerization will be changed, and such effects will have to be taken into account.

SAXS Profiles for PNAM Alone. Fig. S4 shows the SAXS profiles for PNAM alone at the temperature of 70 and 90 °C. The radius of gyration ($R_{g,S}$), the second virial coefficient ($A_{2,PNAM}$), and the cross-sectional diameter (*d*) were determined with the Berry plots (Inset of Figs. S4a and S4b) by using

$$\lim_{c\to 0}\sqrt{\frac{K_e c}{I(q)}} = \frac{1}{\sqrt{M_{w,PNAM}}} + \frac{1}{6}\frac{R_{g,S}^2}{\sqrt{M_{w,PNAM}}}q^2 \tag{S19}$$

$$\lim_{q\to 0}\sqrt{\frac{K_e c}{I(q)}} = \frac{1}{\sqrt{M_{w,PNAM}}} + A_2\sqrt{M_{w,PNAM}}\,c \tag{S20}$$

The obtained values are listed in Table S2. The values at 80 °C were estimated by the interpolation. In the fitting of the SAXS profiles (Fig. 3) with eq 3, the $R_{g,S}$ values obtained for the PNAM alone were used.

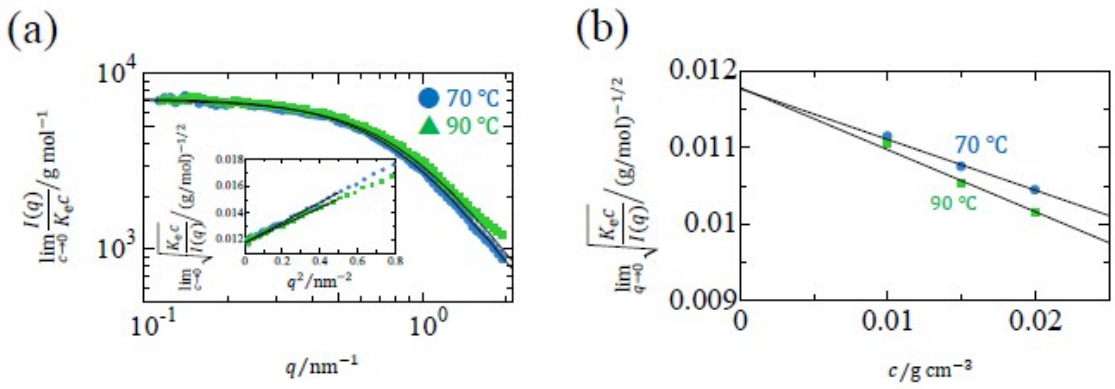

Fig. S5 (a) SAXS profiles of PNAM alone in water as double logarithmic plots. Inset: The same data as the Berry plots. (b) Concentration dependence of the scattering intensity shown as the Berry plots. The blue circles and green squares represent the data at 70 and 90 °C, respectively. The solid curves in panel a represent the fitted model curves by Gaussian chains. The solid lines in panel b and the inset of panel a represent the extrapolating lines.

Table S2. The Parameters for PNAM

T / °C	$R_{g,S}$ / nm	$A_{2,PNAM}$ / cm^3 mol g^{-2}	d / nm
70	2.0	-7.9×10^{-4}	0.5 ± 0.2
80	2.0 [a]	-8.8×10^{-4} [a]	0.5 [a]
90	1.9	-9.7×10^{-4}	0.5 ± 0.2

[a]Estimated by the interpolation of the data at 70 and 90 °C

ρ_S and $c_{w,NAT}$ as Functions of $M_{n,PNAT}$.

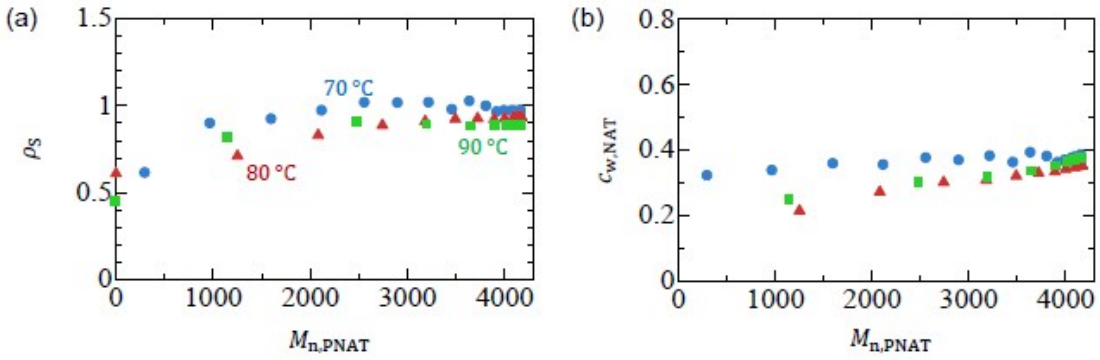

Fig. S6 ρ_S (a) and $c_{w,NAT}$ (b) plotted against $M_{n,PNAT}$ during PISA at 70 (blue circle), 80 (red triangle), and 90 °C (green square).

SAXS profile at a higher concentration. PISA was run at c = 0.055 g/mL in a vial at 70 °C. After that, the *ex situ* SAXS measurement for the solution were performed at 25 °C. The SAXS profile is shown in Fig. S7. The profile exhibits the positive slope at the low-q region, indicating that the structure factor [$S(q)$; inter-micelle interference effect] influences the SAXS profile. If the scattering particles are monodisperse, we have the relationship of $I(q) \propto P(q)S(q)$. Under this assumption, we analyzed the SAXS profile with the Percus-Yevick approximation (hard sphere model) for $S(q)$.[S15] Regarding $P(q)$, the core-corona spherical micelle model was similarly used as in the case of c = 0.01 g/mL. The model nicely fits the experimentally-obtained data as shown in Fig. S7. In this fitting, almost the same values for the fitting parameters as in the case of c = 0.01 g/mL was used for $P(q)$. In particular, the concentration within the core was 0.4±0.01 g/mL. Here, the dispersity obtained by the fitting was narrow ($M_{w,mic}/M_{n,mic}$ = 1.1; *cf.* eq S16), and thus, $I(q) \propto P(q)S(q)$ in this case may be a good approximation and results in the well

fit to the data. Therefore, the micellar structure (the morphology and the concentration within the core) is not significantly different from that at c = 0.01 g/mL.

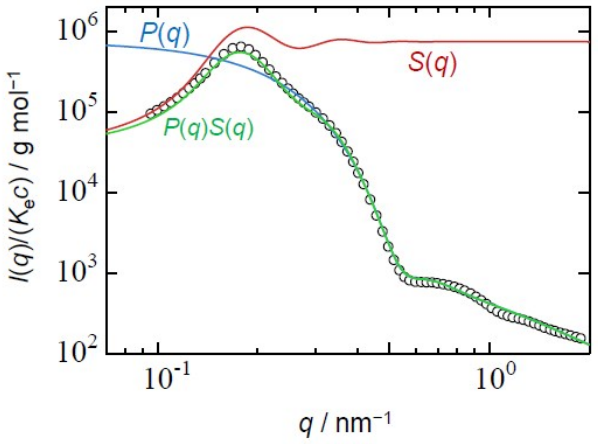

Fig. S7 SAXS profile of P(NAT-*b*-NAM) in aqueous solution at c = 0.055 g/mL. The blue, red, green curves represent the form factor [$P(q)$], structure factor [$S(q)$], and their product [$P(q)S(q)$], respectively.

Numerical Data and Symbols.

Table S3. Numerical data of N_{agg}, R_C, ρ_S, and $c_{w,PNAT}$

T/℃	t/min	$M_{n,PNAT}$	$N_{agg}{}^{a}$	R_C/nm_a	ρ_S	$c_{w,PNAT}/g\ cm^{-3}$
70	5.83	300	7.0±0.4	1.4±0.1	0.61	0.32
	7.85	970	22±2	2.9±0.2	0.90	0.34
	9.99	1600	31±2	3.8±0.2	0.92	0.36
	12.2	2120	43±3	4.7±0.3	0.97	0.36
	14.7	2560	53±3	5.2±0.3	1.0	0.38
	17.2	2900	61±3	5.8±0.3	1.0	0.37
	19.9	3220	66±3	6.0±0.3	1.0	0.38
	22.8	3460	69±3	6.4±0.3	0.98	0.36
	25.8	3640	73±4	6.5±0.4	1.0	0.39
	29.1	3810	75±4	6.7±0.4	1.0	0.38
	32.5	3920	76±4	6.9±0.4	0.96	0.36
	36.1	3995	77±4	6.9±0.4	0.97	0.37
	40.0	4070	77±4	6.9±0.4	0.97	0.38
	44.1	4100	78±4	6.9±0.4	0.97	0.38
	48.4	4150	78±4	7.1±0.4	0.93	0.35
	53.0	4170	79±4	6.9±0.4	0.97	0.38
	57.9	4170	79±4	7.0±0.4	0.95	0.37

	63.1	4170	79±4	6.9±0.4	0.97	0.38
	68.6	4170	79±4	6.9±0.4	0.97	0.38
	74.4	4170	79±4	6.8±0.4	0.97	0.39
80	3.00	0	5.6±0.4	1.0±0.1	0.61	- [b]
	6.00	1250	24±1	3.8±0.2	0.71	0.22
	8.02	2080	40±2	5.0±0.3	0.83	0.27
	10.1	2740	54±3	5.8±0.3	0.89	0.30
	12.2	3180	64±4	6.4±0.4	0.91	0.31
	14.4	3490	70±4	6.7±0.4	0.92	0.32
	16.7	3720	73±4	6.9±0.4	0.93	0.33
	19.0	3890	75±4	7.0±0.4	0.92	0.33
	21.4	4000	76±4	7.1±0.4	0.93	0.34
	23.9	4090	78±4	7.1±0.4	0.93	0.35
	26.4	4120	78±4	7.1±0.4	0.93	0.35
	29.0	4140	78±4	7.1±0.4	0.93	0.35
	31.7	4150	78±4	7.1±0.4	0.93	0.35
	34.5	4170	78±4	7.1±0.4	0.93	0.35
	37.4	4170	78±4	7.1±0.4	0.93	0.35
	40.3	4170	78±4	7.1±0.4	0.93	0.35
90	1.35	0	4.8±0.3	1.2±0.1	0.45	- [b]
	3.37	1150	29±2	3.8±0.2	0.82	0.25
	5.39	2480	60±3	5.8±0.3	0.91	0.30
	7.41	3200	71±4	6.6±0.4	0.89	0.32
	9.44	3650	75±4	6.9±0.4	0.88	0.34
	11.5	3900	77±4	7.0±0.4	0.88	0.35
	13.5	4030	77±4	7.0±0.4	0.88	0.36
	15.5	4100	77±4	7.0±0.4	0.88	0.37
	17.6	4150	77±4	7.0±0.4	0.88	0.37
	19.6	4160	77±4	7.0±0.4	0.88	0.38
	21.7	4180	77±4	7.0±0.4	0.88	0.38
	23.7	4180	77±4	7.0±0.4	0.88	0.38

[a]Determined by the fitting of SAXS profiles by eq 3 with the N_{agg} and R_C values changed. Within the error range, the model curves fit to the experimentally-obtained data points. [b]Could not be calculated because the estimated $M_{n,PNAT}$ value is zero.

Table S4. Symbols of the Physical Parameters and their Definitions

c	Total solute concentration in mass
t	Elapsing time after the heating the solution for the polymerization
T	Temperature during the polymerization
$I(q)$	Absolute scattering intensity (differential scattering cross-section)
q	Magnitude of the scattering vector
λ	Wavelength of the incident X-ray

θ	Scattering angle
K_e	Constant containing the X-ray contrast factor
r_e	Classical electron radius
N_{Av}	Avogadro's constant
γ_{ave}	Average contrast factor of all the solute
γ_{NAT}	Contrast factor of NAT
γ_{poly}	Contrast factor of the polymer
f_C	Contrast factor of the core within the micelle
$p(t)$	Conversion of NAT
α	Exponent in the scattering function [$I(q) \propto q^{\alpha}$]
β	Exponent ($N_{agg} \propto M_{n,PNAT}{}^{\beta}$)
γ	Exponent ($R_C \propto M_{n,PNAT}{}^{\gamma}$)
$C_{NAT}(t)$	Molar concentration of the unreacted monomer (NAT)
$C_{I_2}(t)$	Molar concentration of the initiator
C_{PNAM}	Concentration of PNAM (macro-CTA)
f	Initiation efficiency
k_d	Kinetic constant of the decomposition of the initiator
k_p	Kinetic constant of the propagation
k_t	Kinetic constant of the termination
t_{ind}	Induction time
$w_{NAT}(t)$	Weight fraction of the unreacted monomer (NAT)
$M_{w,mic}(t)$	Weight-average molar mass of the micelle
M_{NAT}	Molecular weight of NAT
$M_{n,PNAT}(t)$	Number-average molecular weight of the PNAT block chain
$M_{n,PNAM}$	Number-average molecular weight of the PNAM block chain
$M_{n,PNAM-b-PNAT}(t)$	Number-average molecular weight of the block copolymer
M_C	Molecular weight of the core-forming block chain
$P_{mic}(q,t)$	Form factor of the micelle
$E_C(q,t)$	Scattering amplitude from the core
$E_S(q)$	Scattering amplitude from the shell
$E_{ch}(q)$	Scattering amplitude from the individual shell chain
N_{agg}	Aggregation number
R_C	Radius of the micellar core
$R_{g,S}$	Radius of gyration of the shell chain
ρ_S	Shell chain density
$c_{w,NAT}$	Segment mass concentration in the core
$\Delta\mu_0$	Standard chemical potential of the micellar formation per chain
η	Interfacial tension parameter
k_B	Boltzmann constant
n	Number of segments
a_s	Segment length

References

(S1) Sobotta, F. H.; Hausig, F.; Harz, D. O.; Hoeppener, S.; Schubert, U. S.; Brendel, J. C. Oxidation-Responsive Micelles by a One-Pot Polymerization-Induced Self-Assembly Approach, *Polym. Chem.* **2018,** *9,* 1593−1602.

(S2) Perrier, S.; Takolpuckdee, P. Macromolecular Design via Reversible Addition–Fragmentation Chain Transfer (RAFT)/Xanthates (MADIX) Polymerization. *J. Polym. Sci. Part A* **2005,** *43,* 5347−5393.

(S3) Bednář, B.; Edwards, K.; Almgren, M.; Tormod, S.; Tuzar, Z. Rates of association and dissociation of block copolymer micelles: Light-scattering stopped-flow measurements. *Makromol. Chem. Rapid Commun.* **1988,** *9,* 785−790.

(S4) Honda, C.; Hasegawa, Y.; Hirunuma, R.; Nose, T. Micellization Kinetics of Block Copolymers in Selective Solvent. *Macromolecules* **1994,** *27,* 7660−7668.

(S5) E. Hecht, H. Hoffmann, Kinetic and Calorimetric Investigations on Micelle Formation of Block Copolymers of the Poloxamer Type. *Colloid. Surf. A* **1995,** *96,* 181−197.

(S6) Goldmints, I.; Holzwarth, J. F.; Smith, K. A.; Hatton, T. A. Micellar Dynamics in Aqueous Solutions of PEO−PPO−PEO Block Copolymers. *Langmuir* **1997,** *13,* 6130−6134.

(S7) Kositza, M. J.; Bohne, C.; Alexandridis, P.; Hatton, T. A.; Holzwarth, J. F. Micellization Dynamics and Impurity Solubilization of the Block-Copolymer L64 in an Aqueous Solution. *Langmuir* **1999,** *15,* 322−325.

(S8) Waton, G.; Michels, B.; Zena, R. Dynamics of Block Copolymer Micelles in Aqueous Solution. *Macromolecules* **2001,** *34,* 907−910.

(S9) Zhu, Z.; Armes, S. P.; Liu, S. pH-Induced Micellization Kinetics of ABC Triblock Copolymers Measured by Stopped-Flow Light Scattering. *Macromolecules* **2005,** *38,* 9803−9812.

(S10) Zhu, Z. Xu, J.; Zhou, Y.; Jiang, X.; Armes, S. P.; S. Liu, Effect of Salt on the Micellization Kinetics of pH-Responsive ABC Triblock Copolymers. *Macromolecules* **2007,** *40,* 6393−6400.

(S11) Lund R.; Willner, L.; Monkenbusch, M.; Panine, P.; Narayanan, T.; Colmenero, J.; Richter, R. Structural Observation and Kinetic Pathway in the Formation of Polymeric Micelles. *Phys. Rev. Lett.* **2009,** *102,* 188301.

(S12) Kalkowski, J.; Liu, C.; Leon-Plata, P.; Szymusiak, M.; Zhang, P.; Irving, T.; Shang, W.; Bilsel, O.; Liu Y. In Situ Measurements of Polymer Micellization Kinetics with Millisecond Temporal Resolution. *Macromolecules* **2019,** *52,* 3151−3157.

(S13) Takahashi, R.; Narayanan, T.; Yusa, S.; Sato, T. Kinetics of Morphological Transition between Cylindrical and Spherical Micelles in a Mixture of Anionic−Neutral and Cationic−Neutral Block Copolymers Studied by Time-Resolved SAXS and USAXS. *Macromolecules* **2018,** *51,* 3654−3662.

(S14) Pedersen, J. S. Scattering Form Factor of Block Copolymer Micelles. *Macromolecules* **1996,** *29,* 1363−1365.

(S15) Kinning, D. J.; Thomas, E. L. Hard-Sphere Interactions between Spherical Domains in Diblock Copolymers. *Macromolecules* **1984,** *17,* 1712−1718.